SSIM 2023 – PM Dight (ed.)

doi:10.36487/ACG_repo/2335_37

Back-analysis of the Bingham Canyon Mine southeast wall: a complex slope failure mechanism called Leo

S Ergun *Rio Tinto, USA*

D Cambio *Rio Tinto, USA*

CP Williams *Rio Tinto, USA*

M Gaida *Rio Tinto, Australia*

K Lawrence *Equilibrium Mining, USA*

T Katsaga *Itasca Consulting Canada Inc, Canada*

L Lorig *Itasca Consulting Group, Inc, USA*

J Weigel *Rio Tinto, USA*

J Gibbs *Rio Tinto, USA*

G Chapin *Rio Tinto, USA*

B Peik *Equilibrium Mining, USA*

S Sankhaneel *Equilibrium Mining, USA*

Abstract

In May 2021, Rio Tinto's Bingham Canyon Mine (BCM) experienced a 19 Mt slope collapse referred to as the 'Leo' failure. Early detection of the initial slope movement and prediction of the collapse by BCM's integrated monitoring systems allowed for safe evacuation of the mine staff and equipment. Datasets collected prior to and during the failure provide an opportunity to study the progression and dynamics of the collapse. Two independent consultants with extensive prior experience at BCM were engaged to expand the understanding and interrogate the sequence of events leading to the Leo failure through back-analysis in FLAC3D® software (Itasca Consulting Group 2020). The objective of the study was to determine mechanisms and develop learnings that could be used to identify and mitigate similar scale inter-ramp failures as future mine pushbacks are evaluated. The consultants each adopted slightly different approaches in characterisation and modelling processes and operated independently under the direction of mine personnel so that findings could be evaluated with reduced bias. Both consultants were successful in achieving the back-analysis requirements set forth. There were many similarities between the final calibrated models. Learnings identified by both teams during the process were shared. Key differences remain between the two successful back-analyses which results in a measure of uncertainty in the understanding of the observed wall response during the failure. This paper outlines the conceptual failure mechanism and definition of calibration targets and describes the independent back-analyses performed by each consultant. By engaging a collaborative team, Rio Tinto was able to achieve a more robust and reliable means to assess current operational decisions and the future mining pushbacks.

Keywords*: back-analysis, complex mechanism, slope movement, open pit, monitoring, calibration, disturbance factor, rock mass strengths, FLAC3D*

1 Introduction

The Bingham Canyon Mine (BCM), owned and managed by Rio Tinto Kennecott (RTK), is an open pit mining operation southwest of Salt Lake City, Utah, in the Oquirrh Mountains, USA. Approximately 18 Mt of copper

have been produced at BCM since production began in 1903. The open pit is currently over 4,570 m wide and approximately 1,325 m deep, representing challenging stress conditions in the geologically complex pit walls (Cambio et al. 2019).

On 31 May 2021, a 457 m-high portion of the southeast wall at the BCM collapsed (Figure 1) in what became known as the 'Leo' failure. Slope movement had been detected for 12 months prior to the failure. Since the first detection, 23.5 Mt of ore had been mined from the slope toe under strict operational geotechnical management and monitoring procedures. All personnel and equipment were removed from the area three days prior to failure. The failure itself was predicted within the hour, three days prior to collapse. There were no fatalities, physical injuries or equipment damage associated with the collapse. The failure comprised approximately 19 Mt of rock and propagated from the pit floor (1,142 m) up to the current Slice 1 operating level at 1,689 m elevation. The remaining failure scarp consisted of failed debris, pseudo-stable degraded rock mass and intact benches. Ergun et al. (2022) used the 3D Particle Flow Code (Itasca Consulting Group 2021) to perform a runout analysis of the Leo failure and improve the understanding of the failure material characteristics (ore grades, material types etc.).

Back-analysis of the Leo failure was undertaken separately to identify the critical controls of the failure mechanism and calibrate relevant material properties for use in forward predictive models of pit wall stability. The back-analysis was undertaken in 3D using FLAC3D v7 (Itasca Consulting Group 2020) to capture the 3D influence of the pit geometry and geology within the slide area (Griffiths & Lane 1999) by two independent consultants. Both consultants have extensive experience performing characterisation, back-analyses and forward predictive modelling at BCM but use slightly different approaches in their processes.

This paper presents a summary of the construction of the Leo 3D numerical model, back-analysis of the failure timeline, the monitoring data utilised for comparison against the back-analysis model predictions and the learnings from this back-analysis to be applied in future modelling efforts for the mine. It also highlights the benefits of having two consultants, each adopting slightly different approaches, as a measure of uncertainty in the understanding of the observed wall response during the failure and reduction of risk in using the models to assess future wall performance.

(a) (b)

Figure 1 (a) Pre-failure surface; (b) Post-failure surface. Post-failure surface shows Leo failure runout

2 Geological setting

The BCM is a porphyry copper-molybdenum-gold deposit in the Oquirrh Mountains, southwest of Salt Lake City near the eastern margin of the Basin and Range Province. The Oquirrh Mountains are predominantly mid- to late Paleozoic siliciclastic and carbonate sedimentary rocks disrupted by the mid-Eocene intrusion of monzonite (MZ) and successive porphyry intrusions (Porter et al. 2012).

The sedimentary units have been subjected to a complex history of metamorphism and deformation; folding and faulting through multiple events including thrusting, extension, relaxation and intrusion. Prominent bedding parallel faults exist throughout the quartzite and limestone units, particularly at the contacts between these two rock types, with kinematic indications of thrust and normal movement in the fault fabrics. These faults vary in thickness and infill material between different horizons and along the fault length itself (Figure 2).

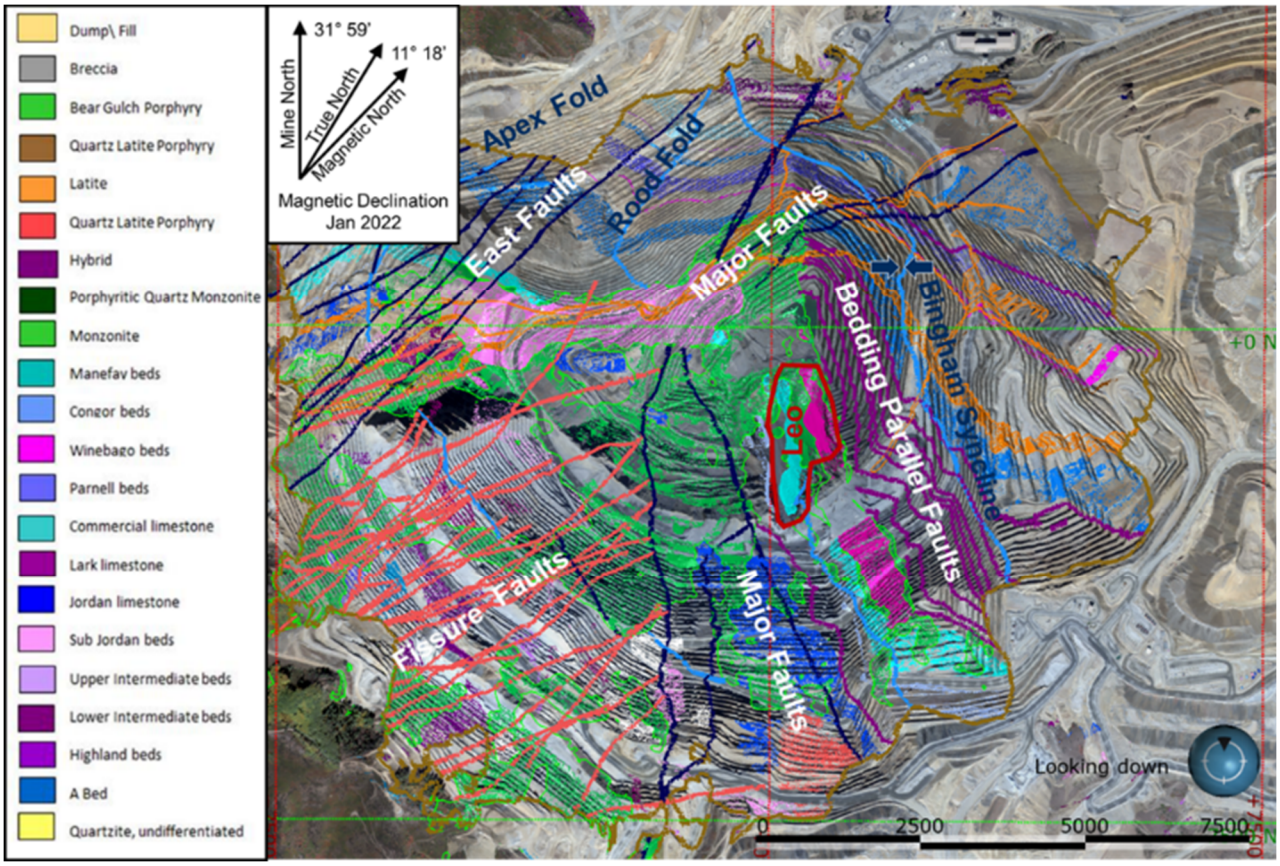

Figure 2 Bingham Canyon Mine geology overview

The Leo failure occurred in the southeast pit wall. Its geology consists of a sedimentary sequence on the west limb of the Bingham Syncline that has been intruded firstly by MZ and then by porphyritic quartz monzonite (PQM). The sedimentary sequence comprises the commercial limestone (COMM) which is massive cherty limestone and mineral-rich garnet skarn. Below the COMM is the Lark Bed, which is composed of limy siltstones and quartzites. The base of the Lark Bed is the Lark Fault. The intrusions cut through the Lark Bed and Lark Fault at the toe of the slope (Figure 3).

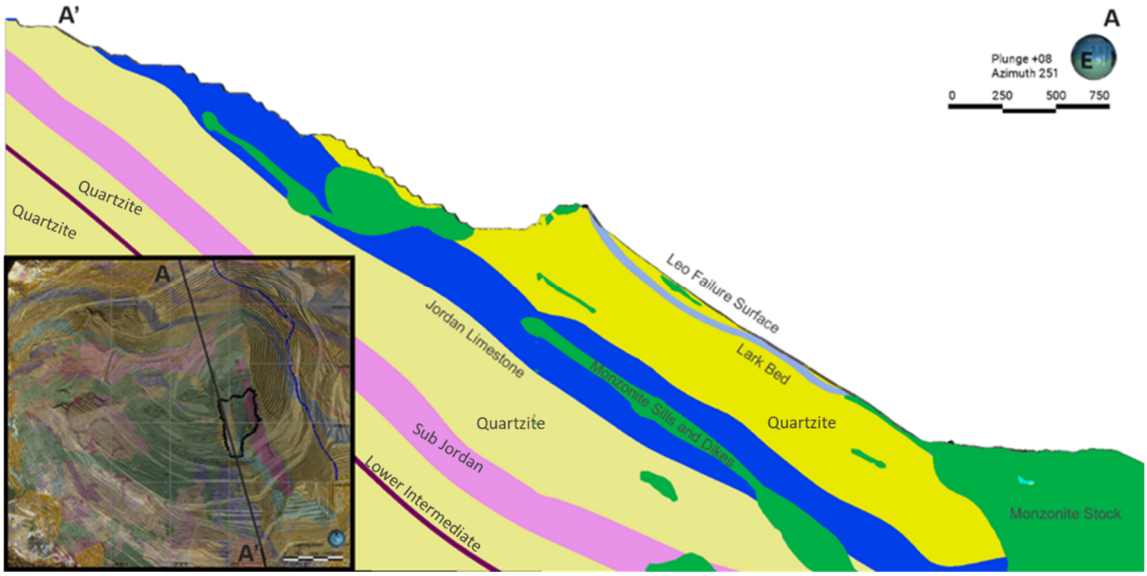

Figure 1 Section through the centre of the Leo area showing the relationship of the sediments to the MZ and the flattening of the dip of the Lark Bed with depth

The Leo failure was controlled on the western side by the Lark Fault. This is an extensional bedding parallel fault that persists over 600 m up the south wall. The eastern release of the failure consisted of a step-path propagation along smooth orthogonal joint sets within the PQM unit. At the toe, the failure propagated through MZ rock mass as a result of mining along the shallower Rebel Fault group set and this was followed by PQM dilation.

The Lark Fault varies from around 0.90 to 0.10 m in thickness and has a number of splays of parallel faults which can be separated 3 to 8 m apart within the Lark limestone bed (Figure 4). The infilling in the Lark Fault varies between clay gouge and sandy materials. Signs of movement are common along the structure. Locally there are also areas of mineralisation, and the Lark Bed was subjected to historical underground mining in adjacent areas to the Leo failure. The fault is interpreted to have formed during compressional events prior to the regional extension approximately coeval to the intrusion of the MZ and PQM resulting in the formation of the Bingham Syncline to the north. There is no evidence that the bedding parallel structure extends into the intrusive rocks adjacent to the Lark Bed, although joints with a similar dip direction, but with steeper dips, are present in the MZ.

The Lark Fault delineates the western limit of the upper part of the Leo failure in the southeast wall of the pit and clearly played a role in defining the upper part of the instability on the western side of the Leo slide. This fault, which parallels the bedding in the Lark and COMM limestones, dips towards the north-northeast (022° azimuth), i.e. at an oblique angle to the north-northwest (335° azimuth) direction to which the wall faces. The fault also flattens somewhat with depth, as shown in Figure 4.

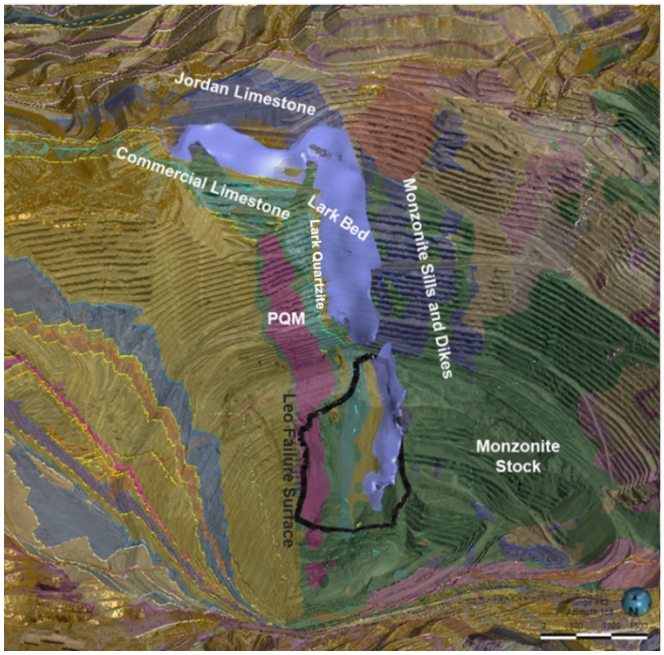

Figure 4 Lithological units in the southeast wall

3 Slope monitoring

The RTK surface monitoring system was active and in place during mining of the Leo sector slopes, and detected the initiation of deformation approximately 12 months prior to the collapse of the wall (Abrahams et al. 2022). The monitored slope deformation indicated that the slope was in an increasing state of deformation from late February 2021. Mining continued at the toe of the Leo sector wall using the observational mining method and 33 Mt of ore was successfully extracted following the detection. Continuous evaluation of the monitoring data resulted in the safe removal of personnel and equipment at the crest and toe three days prior to the collapse of the wall.

The Leo failure movement was detected by multiple slope monitoring methods deployed at the mine, including ground-based radars (RAR and SAR), prisms, GPS units, a thermal camera and InSAR. Tension cracks on the crest of the movement were also visible. The following sections detail the observations from the key monitoring equipment.

3.1 Surface monitoring

Three slope radars located on the north wall provided monitoring data for the Leo movement area, as shown in Figure 5. All three radar units were used to provide detailed real-time monitoring coverage. Robotic total stations were used for monitoring the prisms in the Leo sector. The southeast wall is located below the ARC3 radar unit (refer to Figure 5). Prism coverage on the Leo wall was variable, with a limited number of prisms in the Block 1 sector, as is also shown in Figure 5. These prisms were installed as the slope was developed. However, once movement had been detected on the wall in mid-2020, there was no access to the upper-wall above the current operating level to install additional prisms. This is reflected in the increased prism distribution in the lower benches of Block 2 and Block 3 sectors.

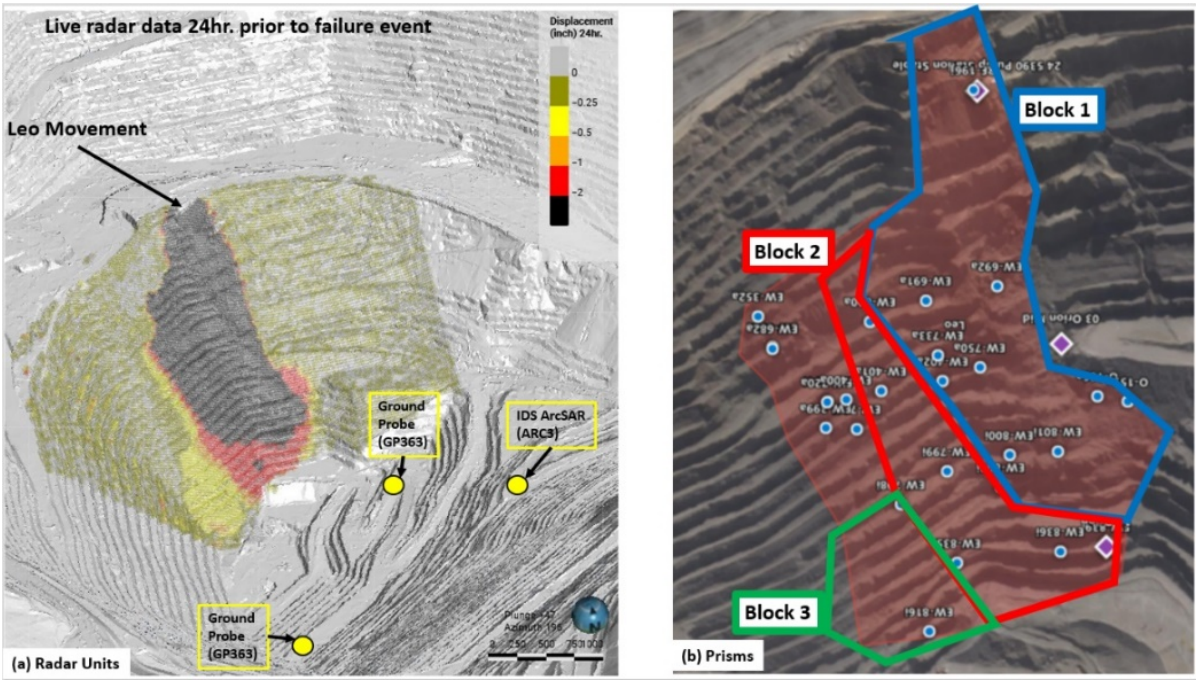

Figure 5 Surface monitoring system for the Leo sector

The monitoring data from the ARC3 unit formed the basis for evaluation of the progression of the slope movement. The ARC3 radar data were analysed in detail on a continuing basis using a subsampling (SS) approach to improve low-level deformation detection. Graphs of surface displacement based on the radar data show the general movement trends in the wall from the initiation of movement in mid-2020. These movement trends form the basis for the model calibration in Figure 6.

The radar monitoring indicated steady creep movements propagating across the slope from the west side, commencing in May 2020, and subsequently extending down the wall following the progression of mining.

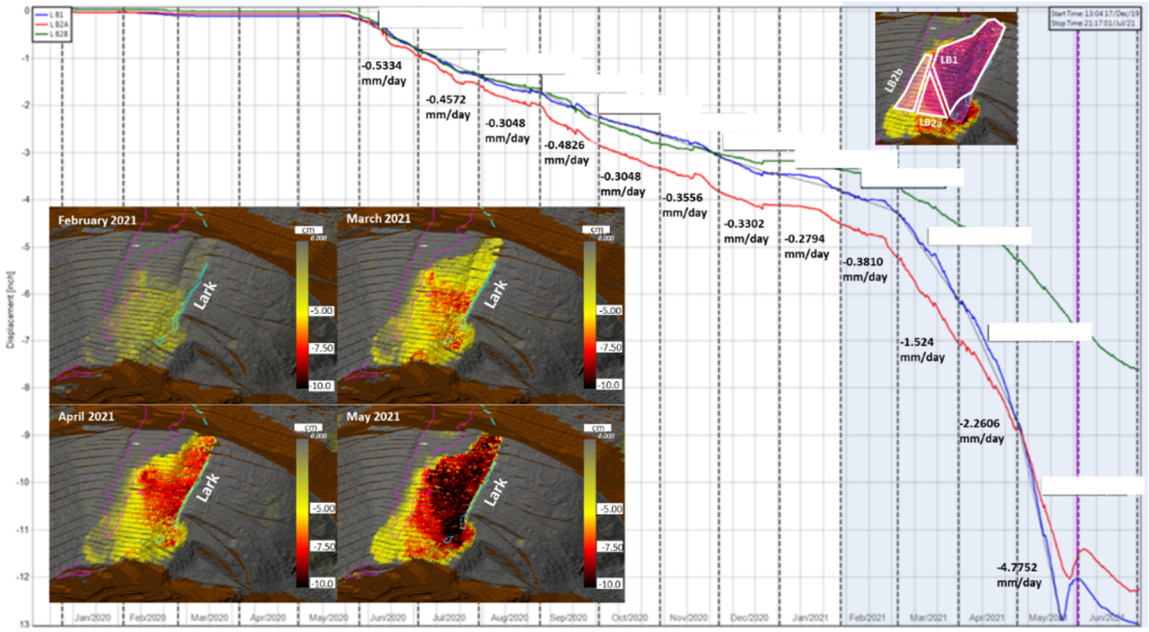

Figure 6 Plot of ArcSAR radar sub-sampled radar data for Leo

During the observational mining period there were indications of sensitivity to blasting and mining at the toe of the wall, with minor increases in movement followed by temporary regressions of the movement. Subsequent to January 2021, the indicated movement rates progressively increased, possibly in response to

the production blast and associated trim blast at the toe of the wall. After the blast the movement rates fluctuated, but at an increasing overall rate in response to the toe of the southeast wall and associated pauses. Eventually the tipping point was reached in late May 2022, by which time the radar-indicated movement rates were more than 10.0 mm/day.

As part of the continuous evaluation of the ARC3 radar data under the Leo trigger action response plan system, the inverse velocity method was used to define the estimated time to failure. When the forecasted time to failure reached three days, full evacuation of the area above and below Leo was appropriately instituted on the afternoon of 27 May, with the failure occurring on the morning of 31 May.

3.2 Thermal camera

Continuous thermal camera video imagery recordings (24 hours per day, 15 frames per second) were available, beginning approximately five days before the Leo failure (Wellman et al. 2022). Thermal infrared cameras detect radiated heat energy and require no visible light (i.e. they provide video imagery in day and night conditions). The selected thermal video camera (Teledyne Forward Looking InfraRed (FLIR) ID-632 z 640 x 480-pixel, security camera) provided a 32° (horizontal) and a 26° (vertical) field of view (Figure 7). The thermal imagery was collected as part of a rockfall detection project of the University of Arizona's Geotechnical Center of Excellence. The entire pre-failure slope of the Leo mechanism was within the thermal camera field of view except for a portion (lower left) of the two lowermost 15 m benches. Toe runout beyond the thermal camera field of view was visible and recorded by mine closed-circuit television (CCTV).

The Leo failure development was tracked using a frame-by-frame interpretation of apparent trajectories of selected positions on several benches that remained relatively intact throughout the late stages of failure (Figure 7a). As shown in Figure 7, both the temperature gradient between warmer faces and colder benches and the resolution of the FLIR imagery facilitated a straightforward and repeatable interpretation of the failure development stages which were used to support Leo sub-block stability targets within the thermal camera field of view. Failure development stages were also interpreted with CCTV video imagery.

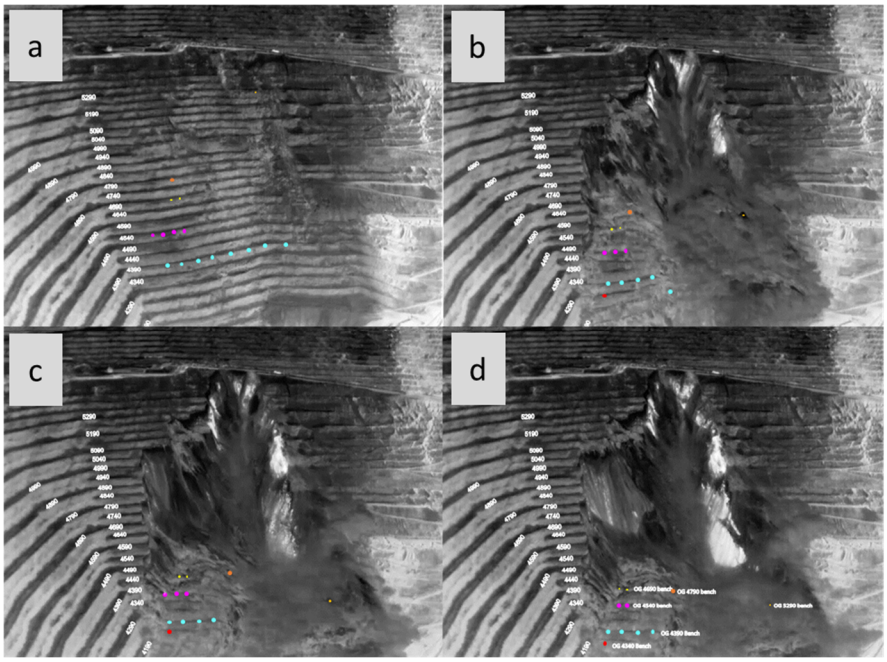

Figure 7 Screenshots of FLIR imagery pre-, during and post-failure, with annotations for benches and colour-coded tracking markers

4 Conceptual failure mechanism

The underlying mechanism generating the Leo deformation, which initiated in May 2020, was investigated by the RTK team using the available monitoring data and failure videos coupled with a detailed review of the lithology, structural and hydrogeology models. The assessment clearly indicated that the operative failure mode was complex. This complexity involved a combination of structural and rock mass strength controls. The operative failure is interpreted to have involved different mechanisms in the various sectors of the eventual slide as illustrated in Figure 8. This conceptual understanding forms the base of the back-analyses.

The interpreted failure mode in the various sectors can be summarised as follows:

- Block 1 sector – Deformation on the Lark Fault at the base of the Lark Bed in the upper central and western areas of the instability appear to have produced critical driving forces for the failure.
- Block 2 sector – The deformation on the Lark Fault is likely to have promoted rock mass failure in the altered MZ intrusive 'passive block' in the lower sectors of the failure. The rock mass failure involved anisotropy provided by planar and wedge configurations related to the slope-parallel bedding and joints in the lower portions of the COMM sedimentary units and shears in the MZ.
- Block 3 sector – Deformation and eventual failure in the western and central part of the slide area are likely to have removed confinement for the eastern side of the slide area, thereby promoting similar fabric-associated rock mass deformation and failure in the intrusive MZ and PQM rocks on the east side of the slide.

This progressive failure mode was evident in the videos of the failure as well as from an analysis of the prism-monitoring data.

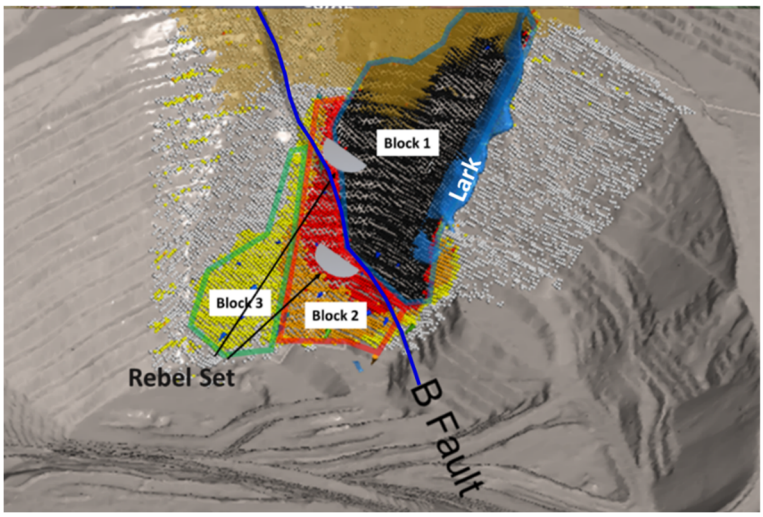

Figure 8 Defined sectors of the Leo slide based on radar data

5 Hydrogeology

A regional groundwater model for the pit was calibrated to support geotechnical design. The groundwater model is built to a scale that incorporates the entire pit, with the extents of the modelling domain stretching from the alluvial sediments in the Tooele Valley across the Oquirrh Mountains that host the mine and over to the sediments of Salt Lake Valley. The framework for the groundwater model is the structures (faults/folds) and geologic units mapped and modelled by the geology team. Piezometer data, pumping fluxes, and fluxes from a horizontal drain and drainage gallery located 121 m behind the toe of the final Slice 2 design are also incorporated into the groundwater flow model. As the model is in a topographic high, all water into the model is in the form of precipitation which occurs as rain and snow. Observational data from 1,378 instruments and data from early 2000 to 2018 are used to calibrate the model for forward predictions.

The groundwater model is considered well calibrated, with over 29,381 porewater pressure calibration target instruments and a scaled root mean square error of 3.3%.

Key findings are summarised as follows:

- Shallow, near pit surface pore pressures are present on the mid-slope area of the South Wall but dissipate over time due to the mining of low conductivity beds and advancement of the overbreak zone of 60 m based on increased fracturing.
- Exposure, from mining, of new hydrogeologic compartments for surface recharge and draining of shallow groundwater may result in temporary pore pressure increases in mid-slope areas that subsequently dissipate.
- Horizontal drains provide depressurisation but residual pore pressure may remain at shallow depths behind the pit slope.

While the groundwater model and calibration are good, the model is not able to represent seasonal variability inducted during snow melt as exhibited by the piezometers. Recognising this inability to capture the seasonal fluctuations due to spring recharge, sensitivity runs are conducted by incrementing the saturated heads by specific values.

In the area of the Leo failure the groundwater model is predicting dry conditions due to the dip of the Lark Bed, the existence of drainage gallery drains near the toe of the slope and the overbreak zone of 60 m. Following the failure of Leo, investigations identified the lower three benches reporting wet blastholes within the Leo failure mass. As the blasthole crews do not have a set depth for water, a wet blasthole could mean 0.3 m or more of water in the hole. Estimates of pore pressure were made based on an increased number of blastholes reporting water. With the increased wet blastholes in the lower three benches, an Ru of 0.1 was applied in the toe of the slope.

A pit-wide review of recharge response was conducted and, based on this evaluation, the average increase in porewater pressure that resulted during snow melt corresponded to a 4 m pressure increase for piezometers at a depth of between 15 and 30 m below ground surface. While there was not any historic water observed on the Lark Fault, an additional 4 m was applied to segments of the Lark Fault to achieve calibration based upon this potential recharge condition.

A combination of Ru in the toe (0.1) and the assumed 4 m of water on the Lark Fault was used for calibration of the geotechnical model.

6 Back-analysis

6.1 Model configuration

Model extents for the two models, chosen to minimise the impact of boundary conditions on the area of interest, are displayed in Figure 9. The most reliable information about principal stress directions comes from the acoustic televiewer (ATV) breakout data due to its consistency over depths and rock types. This data also indicates that the horizontal stresses are not equal: otherwise there would be no identifiable breakouts. The ATV breakout data suggests a major horizontal stress oriented at 123/303 with respect to mine north. The horizontal-to-vertical stress ratios are uncertain, with both consultants adopting the ratio K_H:K_h:K_v of 0.8:0.5:1, as displayed on the inset of Figure 9.

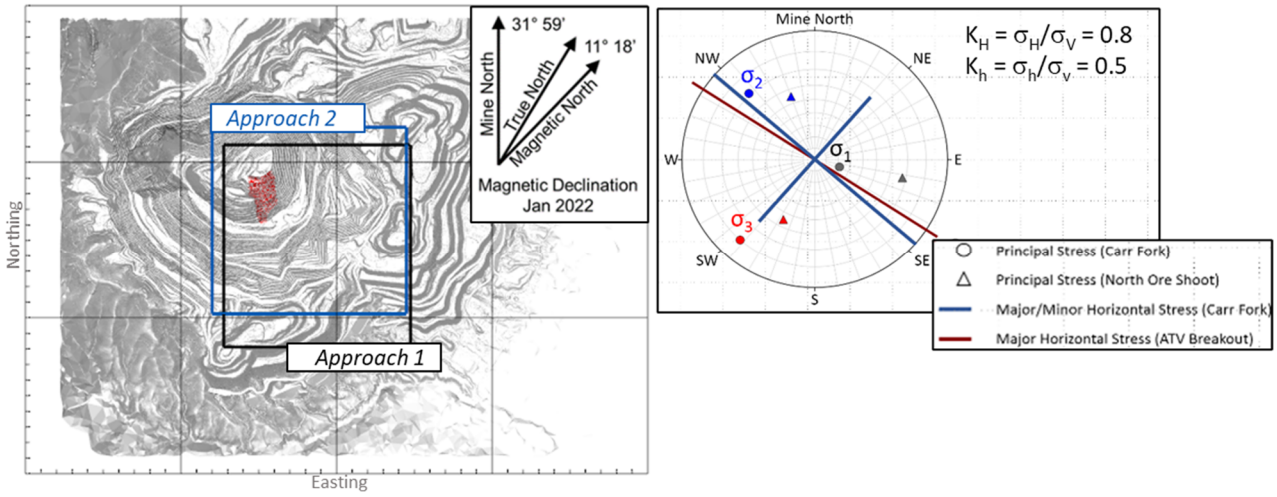

(a) (b)

Figure 9 (a) FLAC3D model extents displayed on 31 May 2021 pit topography; (b) In situ stress condition

6.1.1 Modelling Approach 1: multiple ubiquitous joints

In the first approach, the geology model is discretised using an octree mesh, with a higher resolution defined near all critical contacts, faults and mine sequencing. In the area of the Leo failure, a mesh resolution of 7.6 m (i.e. half a bench), which honours the resolution of the geological strength index (GSI) block model developed at BCM, was adopted. The rock mass behaviour is simulated using a custom multiple ubiquitous joint (MUJ) model which is an extension of FLAC3D's ubiquitous joint (UJ) model (Itasca Consulting Group 2019), developed and validated by the consultant using analytical and numerical verification problems documented in other commercial software (RocScience 2022a, 2022b). Rock mass failure in the MUJ model uses a Mohr–Coulomb failure criteria with up to three anisotropic orientations (with unique strength properties). Equivalent Mohr–Coulomb strengths are updated for the rock mass component as the stress-state evolves, based upon Hoek–Brown curves developed for each geotechnical unit (GTU). The weak plane formulation follows that of the UJ model, which also uses a Mohr–Coulomb failure criteria. Up to three discontinuity orientations are specified for each GTU, based upon detailed structural assessment of critical orientations, with strengths defined based upon the type of discontinuity (joint, fault, bedding). Although the constitutive model supports a strain softening implementation, it was not applied in this application. Faults are represented using the densified weak zone approach and a Mohr–Coulomb failure criterion.

6.1.2 Modelling Approach 2: interfaces and strain softening

The model discretisation was implemented using a fault-conforming grid to represent 17 geological structures explicitly. Conforming grid around faults was created by Griddle (Itasca Consulting Group 2020) using hex-dominant elements. Rock mass behaviour in the Approach 2 model is simulated using a strain softening constitutive model, IMASS (Itasca Consulting Group 2019), with a Hoek–Brown yield criterion. In cases where the joints controlling rock mass strength have a preferred orientation, UJ are utilised with orientations that reflect the true orientation distribution. The strain softening model reduces strength from peak to residual as rock mass shear strain accumulates. Residual strengths are based on Barton rockfill shear strengths, assuming rough and highly interlocked particles. The critical shear strain increment at which the rock mass is reduced to residual is assumed to be GSI dependent. This allows a higher GSI rock mass to be represented as more brittle and a lower GSI rock mass to be modelled as more ductile. All faults in the model are modelled explicitly using an interface approach such that surfaces can slip and separate. The constitutive model for interfaces is defined by a linear Coulomb shear-strength criterion.

6.2 Mining sequence

The mining sequence was modelled by excavating the pit in several stages and solving to equilibrium. The primary time steps included for the Leo failure back-analysis are as follows:

- End of March 2020.
- End of December 2020.
- End of April/May 2021.

Five additional excavation stages were considered between the pre-mining topography and the end of March 2020. Additional back-analyses were completed at the earlier stages to build additional confidence in model performance but have not been included in this paper.

6.3 Calibration criteria

A conceptual understanding of the mechanism was discussed between all parties to gain alignment prior to the commencement of the calibration effort. Observations from slope monitoring and the geological interpretation of the failure area were used to define a set of calibration targets for the numerical models provided in Table 1. These targets were both specific, so that a successful back-analysis could be measured against these pre-defined goals, and less explicit, to allow the parallel approaches employed by the two consulting teams the freedom to derive independent and unbiased conclusions on the critical controls of the mechanism.

Table 1 Calibration targets

Year	Calibration targets
March 2020	Stable slope.
End of Year (EOY) 2020	A decreasing strength reduction factor (SRF) with mining progress in the MZ. Reduced stability in comparison to March 2020. Marginally stable.
April 2021	Deformation patterns spanning the entire failure area. Deformation orientations matching with measured prisms, with uplift at the toe. An SRF ≤ 1 on primary mechanism – Block 1. The full Leo failure mechanism (Blocks 1–3) developing at a higher SRF. Reduced stability in comparison to the March 2020 and EOY 2020 stages.

6.4 Calibration results

Both approaches were considered successful in achieving the calibration targets, with similarities and differences observed in the critical controls and simulated response. The following sections describe the results of the back-analysis for each approach.

6.4.1 Approach 1

All calibration targets were achieved in Approach 1, including the progression of stability from March 2020 to April/May 2021, initiation of the mechanism along the Lark Fault (growing to Block 1) and stronger behaviour of the MZ in the toe. Key model revisions which were introduced to achieve calibration are as follows:

- Reduced Lark Fault strengths, later verified by additional laboratory testing, were introduced to provide the western release (initiation) of the mechanism for Block 1.

- Reduced strength of a moderate west-dipping fault set (F1, dip/dip direction of 63°/265°) and north-dipping (J1, 39°/001°) joint/bedding set (Figure 10a) in the Lark quartzite (LarkQ) sediments on top of the Lark Fault/Bed, which has been observed to generate smaller bench-scale instabilities in previous pushbacks at higher elevations, form the eastern extent of the smaller Block 1 wedge.
- The shallow Rebel Fault set (35°/331°) was included in the eastern MZ to promote a release along the eastern extent of Blocks 2–3, at a higher strength reduction factor (SRF) (Figure 10b).
- The B-Fault set (89°/025°), evident in the MZ, PQM, COMM, and LarkQ units, was included to promote deformation and stability patterns parallel to the similarly oriented line separating Blocks 1, 2 and 3.
- Pore pressures are provided from regional pore pressure grids, with an additional Ru = 0.1 applied in the lower three benches to reflect near-surface water as observed in blastholes and 4 m of pore pressure applied on the Lark Fault, as discussed in Section 5.

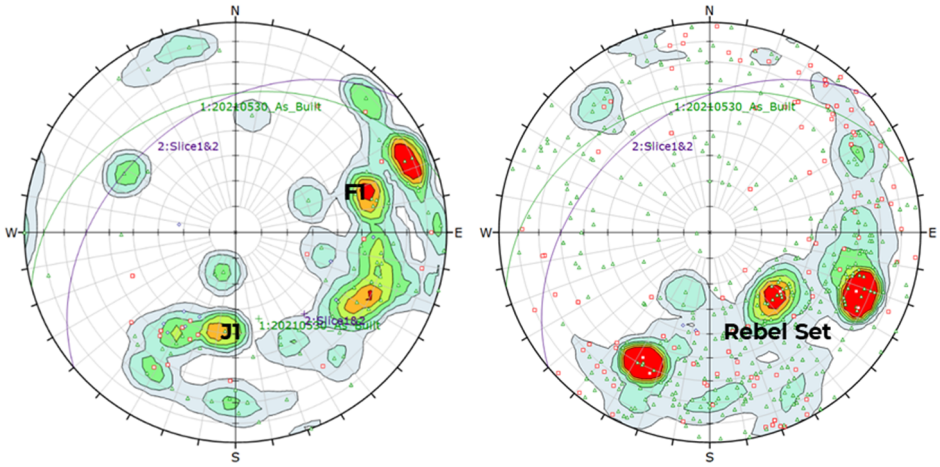

(a) (b)

Figure 10 (a) Lark quartzite and (b) MZ stereonets in the Leo failure area (all surface mapping with 100 ft of May 2021 topography)

The progression in stability of the FLAC3D model for the end of May 2021 stages is displayed using velocity contours for increasing SRF in Figure 11. At SRF = 1.00, the smaller wedge formed by the Lark Fault and anisotropy in the LarkQ is present as observed in the initial failure videos (Figure 11a) and frame-by-frame analysis of FLIR imagery (Figure 7). At SRF = 1.01, the mechanism grows to encompass the Block 1 outline (Figure 11b), including the observed turn in the upper slope as the mechanism passes into the COMM units and across into the MZ/PQM. The Block 2 zone below Block 1 also appears as a transition zone (orange contours) between the unstable Block 1 and more stable Block 3. At an SRF = 1.05 (Figure 11c), the full Leo region is mobilised as the MZ in the toe fails along the shallow, daylighting Rebel set. Note the shape of the mechanism at the lower SRF values (SRF = 1.00–1.01) is reflective of the observed shape of the Leo failure, with the simulated mechanism propagating further east into the PQM at the active mining bench at SRF = 1.05. The model captures the shallow depth of failure and measured volume (~21 Mt), which grows from approximately 14 Mt at SRF = 1.01 to 25 Mt at SRF = 1.05. The slight over-prediction of failure volume is due to the increased instability on the upper eastern side (top left of Figure 11c), where the mechanism progressively fails through the PQM up to the active mining bench.

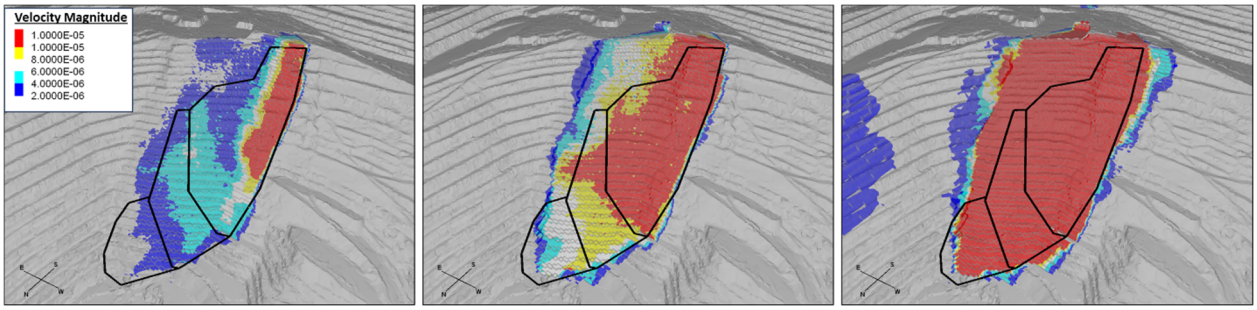

(a) (b) (c)

Figure 11 Simulated failure mechanism progression displayed using velocity contours at the end of the May 2021 stage. (a) Strength reduction factor (SRF) = 1.00; (b) SRF = 1.01; (c) SRF = 1.05

Critical controls on the failure mechanism are illustrated by displaying rock mass and anisotropy failure types on the simulated mechanism (represented by a velocity iso-surface at SRF = 1.05, the red contour of Figure 12c). The geology and major fault overlays are displayed in Figure 12a and Figure 12b, respectively. Figure 12c highlights that the shear along the clay-infilled portions of the Lark Fault (use Figure 12b for reference) forms the western extent of the mechanism, with nearly all the other rock mass yield being associated with faults (parallel to the Lark Fault) intersecting the region. The anisotropy yield overlay (Figure 12 d) identifies several joint sets in the different geological units (reference Figure 12a) as the critical control. MUJ failure is along the shallow Rebel set in the MZ (set S3) and steeper/stronger Rebel oriented set in the PQM (45°/311°, set S2). The shape of the upper Block 1 outline is traced in the dashed black line in Figures 12c and 12 d to illustrate where the transition in the upper slope occurs. The critical sets in the LarkQ unit (F1, 63°/265° and J1, 39°/001°) which form the eastern release of the smaller wedge on the Lark Fault (at SRF = 1.00) are sets S2 and S3 in this unit. in Figure 12d, this presents as either S2 yield (F1, in yellow), S3 yield (J1, green) or both S2/S3 yield (F1/J1, blue). A similar pattern propagates across the COMM unit. At the toe, multiple or all sets yield in combined UJ shear as the mechanism daylights.

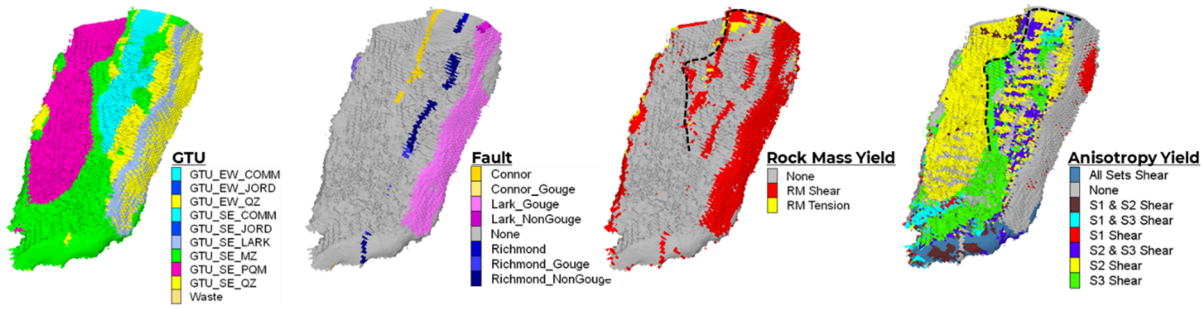

Figure 12 Geology, faults, rock mass yield and anisotropy yield displayed on the simulated failure surface (represented by velocity iso-surface)

Note that in the MUJ approach, the Leo failure is dominated by shear along the Lark Fault in the west and primarily through anisotropy in all other units. Sensitivities conducted throughout the study indicate that rock mass strengths account for less than 5–10% of the resistance along the surface, with the mechanism dominated by UJ shear. It is noted, however, that including multiple directions of weakness in the MUJ model may be replicating the behaviour of a weaker rock mass unit at shallower depths.

6.4.2 Approach 2

The Approach 2 model replicated the failure mechanisms and achieved all calibration targets. The overall Leo mechanisms included sliding along Lark, and shearing and enhanced dilation along MZ and PQM contacts (Figures 13, 14 and 15). The primary controls of Leo failure mechanisms observed in the model were:

- The increased deformation pattern closely replicates the radar SS outline (see Figures 13a and 13b). The decreased stability trend is observed with mining activity starting from March 2020. Sliding along the Lark Fault initiates failure along the southern portion of Block 1 (Figure 14c).
- Lark sliding allows shearing and dilation along PQM and MZ contacts (Figures 14a and 14b). Shearing through the toe in Block 2 is accommodated by UJ in MZ as shown in Figure 15b.
- The lower part of Block 3 movement is initiated by mining in the area with a shallower joint set orientation (37°/341°) in the MZ.
- The model captures a relatively shallow depth of failure and measured volume of 19 Mt. Modelled failure volume is 16 Mt at SRF below 1.00 and 25 Mt at SRFs below 1.05 (Figure 15c).

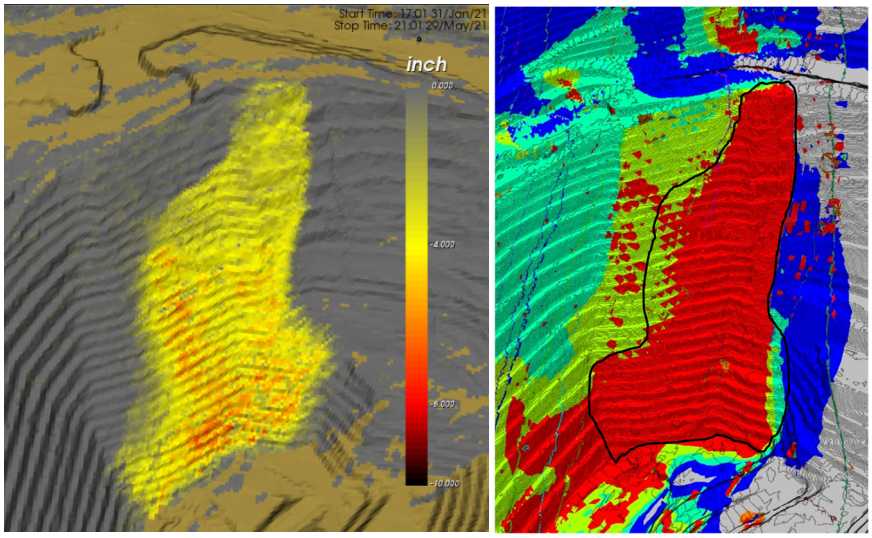

(a) (b)

Figure 13 (a) Radar SS; (b) Horizontal deformations from EOY2020 to April 2021

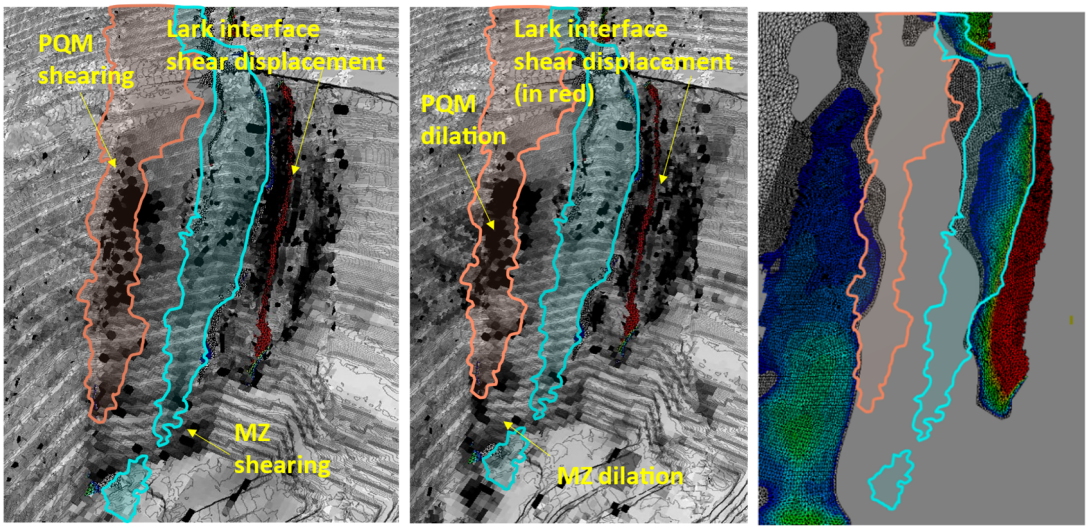

(a) (b) (c)

Figure 14 (a) Rock mass shear strain (darkness is increased shearing) and shear displacement on interfaces (red); (b) Rock mass bulking (darkness is increased shearing) and shear displacement on interfaces (red); (c) Shear displacement contours on the Lark Fault interface

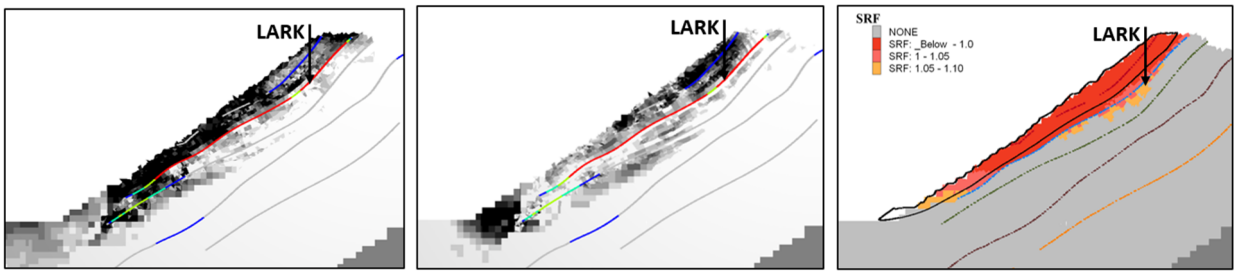

(a) (b) (c)

Figure 15 Cross-section: (a) Rock mass shearing (darkness is increased shearing) and shear displacement on interfaces (red); (b) UJ Shearing (darkness is increased shearing) and shear displacement on interfaces (red); (c) SRF contours and observed failure volume

The following key model refinements were made to best meet the model calibration targets:

- Damaged rock halos with residual properties were introduced along the MZ and PQM contacts, as well as around Lark and other major faults.
- Critical joint orientations were selected through critical review of joint data and sensitivity studies.
- UCS values were assigned considering logged defect intensity that has an effect on the intact block strength (see Hoek & Brown 1980).
- Zones with GSI below 25 were simulated as perfectly plastic material.
- The lower three benches were assigned water pressures with an Ru of 0.1 to reflect near-surface water as observed in blastholes and 4 m of water pressure were applied to the Lark Fault, consistent with Section 5.

6.5 Comparison with monitoring data

The stability of the different blocks is highlighted by comparing the SRF margins of the simulated MUJ and strain softening approaches to the ARC3 radar data in Figure 16. Both back-analyses simulate an initial release along the Lark Fault, with the mechanism growing to encompass the Block 1 region at a minimal increase in SRF (+0.01 in the MUJ approach, +0.05 in the SS approach). Blocks 2–3 are then mobilised as the failure propagates through the MZ and PQM along the eastern extent at higher SRFs (SRF = 1.05 in the MUJ approach, and SRF = 1.10 in the SS approach). The extent of the simulated failure mechanism (in both approaches) in the west spreads further up the wall than observed within the PQM, to the active mining bench; an observation that would be difficult to simulate numerically without a discrete structure which would limit the progressive failure of the mechanism.

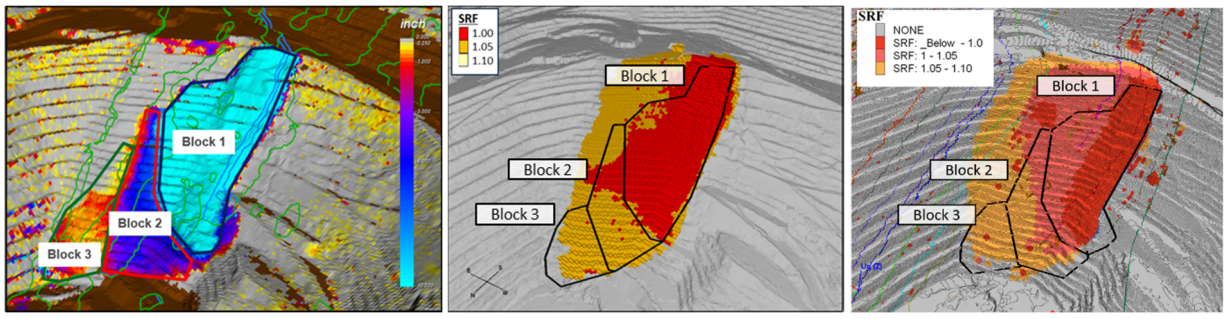

(a) (b) (c)

Figure 16 Leo failure back-analysis – April 2021. (a) ARC3 radar, 1–31 May 2021; (b) Approach 1 – MUJ; (c) Approach 2 – strain softening

Figure 17 presents the movement direction, recorded by active prisms in the Leo area, compared to the simulated deformation at these locations from December 2020 to April 2021. Both models capture the direction of observed movement reasonably well and replicate the observed heave in the toe of the Leo mechanism.

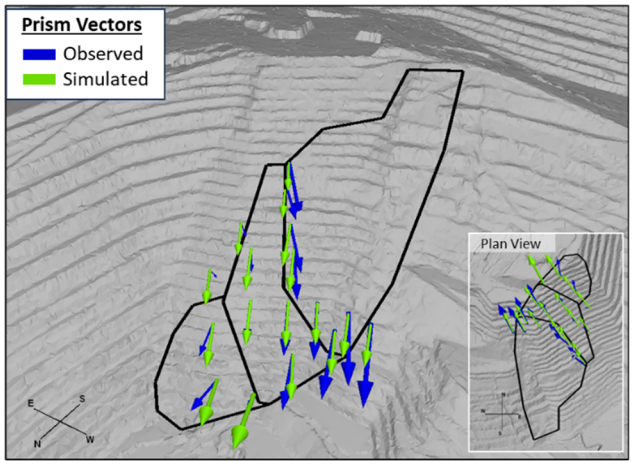

(a)

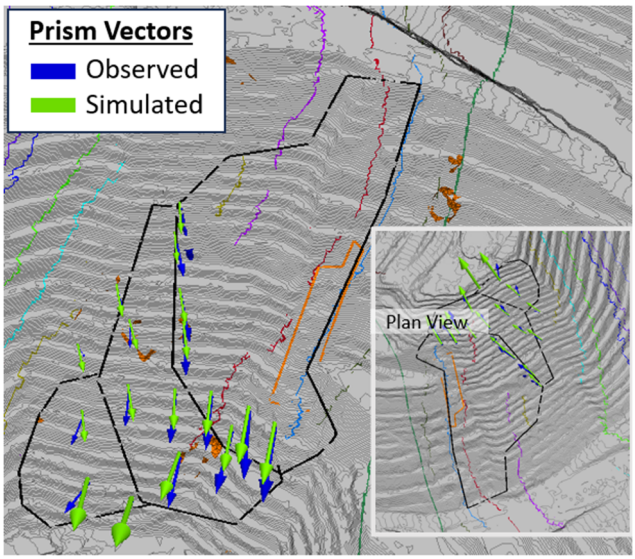

(b)

Figure 17 Observed and simulated deformation at prism locations (end of December 2020 to end of April 2021). (a) Approach 1 – MUJ; (b) Approach 2 – strain softening

7 Conclusion

Early detection of the initial slope movement and prediction of the Leo failure provided the opportunity to collect a unique dataset that could be used study the progression and dynamics of the collapse. The data was used to develop a conceptual understanding of the failure mechanism which subsequently formed the basis of parallel back-analyses, conducted by two independent consulting groups. The consultants applied separate approaches in their respective back-analysis, but both studies were considered successful, with merits and limitations of both. Key differences in the modelling approach and results from the current analysis are summarised in Table 2.

Table 2 Summary of approach and results

Component	Approach 1	Approach 2
Constitutive model	MUJ	IMASS strain softening with UJ
Mesh	Octree, 7.6 m finest resolution	Octree and hex-dominant meshing around faults using Griddle
Faults	Weak densified zone approach, with gouge/non-gouge strength puddles	Interface representation of faults, with gouge/non-gouge strength puddles
Rock mass	Hoek–Brown	Hoek–Brown, with residual strength
Anisotropy	Up to three, with Mohr–Coulomb yield	Single, with Mohr–Coulomb yield
Timeline	Both models capture the progressive reduction in stability from March 2020 to April/May 2021	
Failure mechanism	Initiation along the Lark Fault and LarkQ anisotropy in the west, extending to PQM and passive MZ block at SRF = 1.05, exploiting Rebel Fault group anisotropy	Sliding along Lark, presented as a discrete feature, shearing and dilation along PQM and MZ contacts. Shearing through the toe in Block 2 is accommodated by anisotropy in MZ
Failure shape	Transition of Blocks 1, 2 and 3 evident at increasing SRF (1.00–1.05) Excellent agreement, with higher SRFs progressing further upslope to the active mining bench	Blocks 1, 2 and 3 are captured through the deformation pattern and SRFs (1.00–1.10) Excellent agreement on failure depth and failed volume
Deformation data	Agrees well will with pre-failure radar and prism data (direction and magnitude), including toe heave in the passive MZ block	Replicates radar SS distribution and prism data (direction and magnitude), including toe heave in the passive MZ block

The analyses were able to replicate the progressive reduction in stability from March 2020 through to the eventual collapse in May 2021, within primary initiation due to sliding along the Lark Fault. There were also differences noted, including in the estimation of the stability margins and interpretation of critical controls which enable the propagation of Block 1 towards the east through the MZ and PQM. This strategy of parallel studies by RTK provides for a comprehensive understanding of the Leo failure mechanism, and an enhanced capacity for evaluating future design options and mitigating potential failure mechanisms with similar controls.

Acknowledgement

The authors would like to thank RTK management and legal for support in the development of this content, and the modelling teams at WSP, RockTech Mining and Itasca Consulting Group who have contributed to this content. In addition, the authors would like to thank the reviewers for their thoughtful comments and efforts towards improving this manuscript.

References

Abrahams, G, Morkeh, J & Telfer, J 2022, 'Mining above and below a large failure scarp at the Bingham Canyon Mine', *Proceedings of Slope Stability Symposium 2022*, University of Arizona, Geotechnical Centre of Excellence, Tucson.

Cambio, D, Hicks, DD, Moffit, K, Yetisir, M & Carvalho, JL 2019, 'Back-analysis of the Bingham Canyon South Wall: a quasi-static complex slope movement mechanism', *Rock Mechanics and Rock Engineering*, vol. 52, pp. 4953–4977, https://doi.org/10.1007/s00603-019-01958-7

Ergun, S, Emam, S, Rodriguez, P, Fahle, L, Schafer, K, Dedecker, F, … & Ross B., 2022, 'Particle flow code modelling of slope failure and runout at Bingham Canyon Mine', *Proceedings of Slope Stability Symposium 2022*, University of Arizona, Geotechnical Centre of Excellence, Tucson.

Griffiths, DV & Lane, PA 1999, 'Slope stability analysis by finite elements', *Geotechnique*, vol. 49, pp. 387–403, http://dx.doi.org/10.1680/geot.1999.49.3.387

Hoek, E & Brown, ET 1980, 'Empirical strength criterion for rock masses', *Journal of Geotechnical and Geoenvironmental Engineering,* vol. 106, no. GT9, pp. 1013–1035.

Itasca Consulting Group Inc 2019, *FLAC3D — Fast Lagrangian Analysis of Continua in Three-Dimensions*, version 7.0, computer software, Itasca, Minneapolis.

Itasca Consulting Group Inc 2020, *Griddle — Advanced Meshing Tools for Numerical Modelling*, version 2.0, computer software, Itasca, Minneapolis.

Itasca Consulting Group Inc 2021, *PFC — Particle Flow Code*, version 7.0, computer software, Itasca, Minneapolis.

Porter, JP, Schroeder, K & Austin, G 2012, *Geology of the Bingham Canyon Porphyry Cu-Mo-Au Deposit, Utah, Geology and Genesis of Major Copper Deposits and Districts of the World: A Tribute to Richard H. Sillitoe.*

RocScience Inc 2022a, *RS2 – 2D Finite Element Program for Stress Analysis and Support Design Around Excavations in Soil and Rock*, version 11, computer software, Rocscience, Toronto.

Wellman, EC, Schafer, KW, Williams, CP & Ross, BJ 2022, 'Thermal imaging for rockfall detection', *Proceedings of the US Rock Mechanics/Geomechanics Symposium*, American Rock Mechanics Association, Alexandria.